The three-electron bond =Si<O2:·Yb absorption center of pre-darkened ytterbium-doped silica

Mattsson, Kent Erik

Published in:
Optics Express

Link to article, DOI:
10.1364/OE.21.012849

Publication date:
2013

Document Version
Publisher's PDF, also known as Version of record

The three-electron bond $=Si<O_2:\cdot Yb$ absorption center of pre-darkened ytterbium-doped silica

Kent E. Mattsson*

DTU Fotonik, Technical University of Denmark, Ørsteds Plads 343, DK-2800 Kgs. Lyngby, Denmark
**KEEM@fotonik.dtu.dk*

Abstract: The formation and bleaching of color centers during annealing of pre-darkened ytterbium-doped silica fibers is modeled by three-electron bond (TEB) = $Si<O_2:\cdot Yb$ absorption centers. The nature of a center and underlying mechanism for its annealing in formation, shift and dissociation of chemical bonds is described in terms of a Markov statistical model with state change set by Bose-Einstein phonon statistics. The center hold one terminal and four active states with activation energies for transitions among these found to match bond energies of molecular oxygen in ionic character bonds of 1 and 1½ bond order. Experimentally observed in- and decrease in absorption during ramp and isothermal annealing of pre-darkened ytterbium co-doped silica fibers are hereby matched by a set of = $Si<O_2:\cdot Yb$ centers.

OCIS codes: (060.2290) Fiber materials; (060.2320) Fiber optics amplifiers and oscillators.

References and links

1. Y.-S. Liu, T. C. Galvin, T. Hawkins, J. Ballato, L. Dong, P. R. Foy, P. D. Dragic, and J. G. Eden, "Linkage of oxygen deficiency defects and rare earth concentrations in silica glass optical fiber probed by ultraviolet absorption and laser excitation spectroscopy," Opt. Express **20**(13), 14494–14507 (2012).
2. K. E. Mattsson, "Photo darkening of rare earth doped silica," Opt. Express **19**(21), 19797–19812 (2011).
3. S. Yoo, C. Basu, A. J. Boyland, C. Sones, J. Nilsson, J. K. Sahu, and D. Payne, "Photodarkening in Yb-doped aluminosilicate fibers induced by 488 nm irradiation," Opt. Lett. **32**(12), 1626–1628 (2007).
4. M. Engholm and L. Norin, "Preventing photodarkening in ytterbium-doped high power fiber lasers; correlation to the UV-transparency of the core glass," Opt. Express **16**(2), 1260–1268 (2008).
5. L. Skuja, "Optically active oxygen-deficiency-related centers in amorphous silicon dioxide," J. Non-Cryst. Solids **239**(1–3), 16–48 (1998).
6. S. Girard, Y. Ouerdane, B. Tortech, C. Marcandella, T. Robin, B. Dadier, J. Baggio, P. Paillet, V. Ferlet-Cavrois, A. Boukenter, J.-P. Meunier, J. R. Schwank, M. R. Shaneyfelt, P. E. Dodd, and E. W. Blackmore, "Radiation Effects on ytterbium- and Ytterbium/erbium-Doped Double-Clad Optical Fibers," IEEE Trans. Nucl. Sci. **56**(6), 3293–3299 (2009).
7. T. Deschamps, H. Vezin, C. Gonnet, and N. Ollier, "Evidence of AlOHC responsible for the radiation-induced darkening in Yb doped fiber," Opt. Express **21**(7), 8382–8392 (2013).
8. R. Schnadt and J. Schneider, "The Electronic Structure of the Trapped-Hole Center in Smoky Quartz," Phys. Kondens. Materie **11**, 19–42 (1970).
9. S. Jetschke and U. Röpke, "Power-law dependence of the photodarkening rate constant on the inversion in Yb doped fibers," Opt. Lett. **34**(1), 109–111 (2009).
10. S. Yoo, A. J. Boyland, R. J. Standish, and J. K. Sahu, "Measurement of photodarkening in Yb-doped aluminosilicate fibres at elevated temperature," Electron. Lett. **46**(3), 233–244 (2010).
11. M. J. Söderlund, J. J. Montiel i Ponsoda, J. P. Koplow, and S. Honkanen, "Heat-induced darkening and spectral broadening in photodarkened ytterbium-doped fiber under thermal cycling," Opt. Express **17**(12), 9940–9946 (2009).
12. M. Leich, U. Röpke, S. Jetschke, S. Unger, V. Reichel, and J. Kirchhof, "Non-isothermal bleaching of photodarkened Yb-doped fibers," Opt. Express **17**(15), 12588–12593 (2009).
13. M. J. Söderlund, J. J. Montiel i Ponsoda, J. P. Koplow, and S. Honkanen, "Thermal bleaching of photodarkening-induced loss in ytterbium-doped fibers," Opt. Lett. **34**(17), 2637–2639 (2009).
14. L. Pauling, "The nature of silicon-oxygen bonds," Am. Mineral. **65**, 321 (1980).
15. V. O. Sokolov and V. B. Sulimov, "Threefold coordinated oxygen atom in silica glass," J. Non-Cryst. Solids **217**(2–3), 167–172 (1997).
16. C. C. Robinson and J. T. Fournier, "Co-ordination of Yb^{3+} in phosphate, silicate, and germinate glasses," J. Phys. Chem. Solids **31**(5), 895–904 (1970).

#187713 - $15.00 USD Received 25 Mar 2013; revised 7 May 2013; accepted 10 May 2013; published 17 May 2013

17. D. L. Griscom, E. J. Friebele, K. J. Long, and J. W. Fleming, "Fundamental defect centers in glass: Electron spin resonance and optical absorption studies of irradiated phosphorous-doped silica glass and optical fibers," J. Appl. Phys. **54**(7), 3743–3762 (1983).
18. P. H. Krupenie, "The spectrum of molecular oxygen," J. Phys. Chem. Ref. Data **1**(2), 423–534 (1972).
19. Table of periodic properties of the Elements, Sargent-Welch, Skokie, IL, (1980).
20. A. V. Kimmel, P. V. Sushko, and A. L. Shluger, "Structure and spectroscopic properties of trapped holes in silica," J. Non-Cryst. Solids **353**(5-7), 599–604 (2007).
21. A. F. Holleman, E. Wiberg, and N. Wiberg, *Inorganic Chemistry* (Academic Press, 2001) p.131.
22. K. Arai, H. Namikawa, K. Kumata, T. Honda, Y. Ishii, and T. Handa, "Aluminum or phosphorous co-doping effects on the fluorescence and structural properties of neodymium-doped silica glass," J. Appl. Phys. **59**(10), 3430 (1986).
23. M. J. Söderlund, J. J. Montiel i Ponsoda, J. P. Koplow, and S. Honkanen, "Thermal bleaching of photodarkening in ytterbium-doped fibers," Proc. SPIE **7580**, 75800B, 75800B-8 (2010).

1. Introduction

The long term stability of amplifiers and lasers is critically influenced by photodarkening (PD) with time dependent broadband loss centered at visible wavelengths and a long tail extending into the near infrared. Several mechanisms and species potentially responsible for PD and the herewith associated PD color center (CC) have been proposed as discussed in [1,2] but a definitive explanation for the process remains a subject of debate.

In [1] a linear dependency for pristine Yb and Er-doped fibers between type II oxygen deficiency center (ODC(II)) absorption at 245 nm (5.06 eV) and rare earth number density is found. The direct ODC(II) to Yb emission excitation in these fibers is in [1] seen as either direct ODC(II) to Yb excitation transfer or that ODC(II) and Yb emission hold a common origin for UV excitation. The growing Tm^{3+}/Er^{3+} trace impurity emission found to follow increase of PD in [2] collaborate this.

In [3] Yb/Al co-doped preform material show 220 nm (5.63 eV) absorption and excitation by 488 nm light which leads to broadband PD loss as well as increased 220 nm absorption. This result is in [3] explained by Yb ions preferably occupying oxygen-surrounding voids created by Al with tetrahedral or octahedral coordination. As the number of Yb ions by co-doping goes beyond the available voids in the silica matrix the possibility of ill-valence bonds between cations (Yb-Al or Yb-Yb) increases. These ill-valence bonds resemble Ge-Ge or Ge-Si bonds in Ge-silicate glasses in that they originate from a deficiency of oxygen [3]. In [4] preform Yb/Al material is found to show ≈230 nm (≈5.4 eV) centered absorption proposed to be due to charge transfer bands of Yb.

The difference between observed centers of [1,3] and [4] is in [1] proposed to be due to drawing induced ODC(II) measured on drawn fibers whereas [3,4] are for preform material. It is further in [1] hinted at that ODC(II), the E' center and non-bridging oxygen hole center (NBOHC) all are participants in UV-induced defect inter conversion processes [5] that provides one potential avenue for PD in Yb/Al fibers. The E' center and NBOHC hold, respectively, 5.6 – 5.7 eV and ≈4.8 eV in center absorption [5].

In [6] X-ray exposed Yb/Al, Yb/P and P co-doped silica fibers are characterized. Here it is found that the Yb/P fiber with 4 times higher Yb concentration and identical broadband 870 – 1100 nm absorption shows half the ≈5.1 eV absorption than the Yb/Al fiber. The Yb/P fiber show increased absorption at ≈1600 nm which is identified as the P_1 phosphorous defect [6]. In [4] an Yb/P fiber with 4.5 times higher Yb concentration show identical slope and half the 700 – 1000 nm absorption than an Yb/Al fiber. The ODC(II) paved PD avenue may therefore also apply for Yb/P fibers – but with a changed ODC(II) to Yb number density relation.

The for lasers and amplifiers operating in the near infrared important CC loss centered at visible wavelengths with long tails extending into the near infrared has not been quantified. In [3] the PD loss is proposed to be due to Yb-Al or Yb-Yb ODC centers while [4] propose it to be due to oxygen hole centers (OHCs) linked to Al or P. In [7] Al OHCs are observed upon γ-ray exposure to hold spectral absorption as found after PD by IR pumping. In this paper an alternative to the ODC/OHC controversy is given by proposing that the valence imbalance

#187713 - $15.00 USD Received 25 Mar 2013; revised 7 May 2013; accepted 10 May 2013; published 17 May 2013

between X (Yb^{3+}, Al^{3+} or P^{5+}) and Si^{4+} is met by three-electron bonds (TEBs) formed between X and pairs of oxygen of XO_4 or XO_6. The traditional view on Al OHCs is that a hole resonates over the AlO_4 unit [8]. The OHC may, however, as well be described as a TEB (two resonant bonds by three electrons). For two TEBs of opposite spin in a shared edge of two adjacent XO_4 or XO_6 units a TEB↑ to TEB↓ bond may form in an interaction that then resembles the link of a weakly bond ODC.

The dynamic behavior of the PD loss makes its characterization challenging. In [9] the PD process is found to demand 5 – 6 eV in activation energy (E_A) or what correspond to 4 - 5 excited Yb ions. In [10] dynamic color center bleaching is found to show 0.07 eV in E_A with full recovery of the induced PD for fibers operating at 573 K. The photochemical reaction mechanisms for the active pumped fibers relies on the actual level of pump absorption, temperature, fiber geometry and Yb ion concentration. To distinguish the different mechanisms involved in the PD process it appears therefore advantageous to analyze the bleaching of pre-darkened fibers by annealing as the relaxation reaction hereby only relies on fiber temperature. This opens for the possibility to directly relate observed change in absorption with activation energy. For pre-darkened fibers an unexpected increase in PD absorption is hereby observed for annealing ramps from room temperature to about 350-450 K followed by the expected bleaching that initiate at 470-600 K [11,12]. Thermally induced PD absorption is not observed for pristine fibers [12] while PD bleaching shows E_A of ≈1.3 eV [12,13] to 1.5 eV [13] dependent on fiber composition and manufacturing condition.

In this paper the CC in Yb/Al and Yb/Al/P material is proposed to be due to a TEB formed between dioxasilirane and Yb (= $Si<O_2:\cdot Yb$). The CC is described through an analogy between polarized TEBs of = $Si<O_2:\cdot Yb$ and polarized TEBs found as an intermediate bond between ½ (1) bond order molecular oxygen and 1 (1½) bond order super-oxide. The interpolated bond energies found hereby are along with Bose-Einstein phonon statistics applied to develop a Markov chain statistical model for annealing of pre-darkened fibers. This model gives good match to the annealing data from [11–13] for a distributed set of CC sites of individual TEB polarization.

2. The ionic character of PD color centers

In a previous work [2] the CC PD absorption is proposed to involve dissociation of superoxide bonds comprising a σ-bond ("1") in parallel to a polarized TEB↑ to Yb as shown in Fig. 1(a) state II↑ ("1+TEB↑"). A further state of the CC is shown in Fig. 1(b) where a "½" bond in parallel to a polarized TEB↑ to Yb forms state iii↑ ("½+TEB↑"). A TEB of two anti-bond parallel spin electrons and one bond electron of opposite spin is denoted TEB↓ and three parallel spins is denoted TEB↑ (anti-bond) which gives two states for each TEB. For pre-darkened fibers the active CCs are taken to be in either state II or iii. The difference in spectral appearance of Yb/Al and Yb/P co-doped material upon PD is in [2] seen as result of change in the type of bonds involved in the CCs. This is here proposed to be due to different TEB ionic character (degree of polarization) in CCs of different sites.

#187713 - $15.00 USD Received 25 Mar 2013; revised 7 May 2013; accepted 10 May 2013; published 17 May 2013

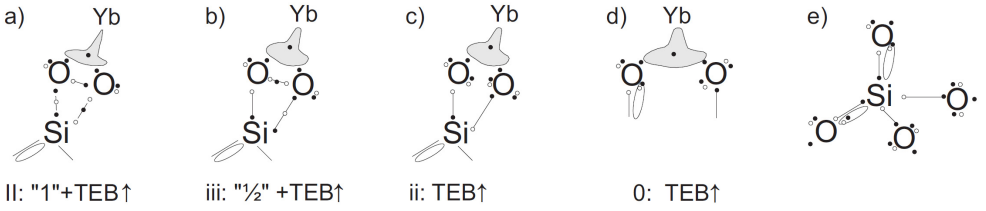

Fig. 1. **(a)** CC state II with two 0.5 bond order Si-O interactions (⋯) and oxygen in σ-bond parallel to a TEB link ("1+TEB"), **(b)** CC state iii with one 1.55 and one 0.5 bond order Si-O interaction and oxygen in "½" bond parallel to a TEB link ("½+TEB"), **(c)** terminal state ii TEB link, **(d)** terminal state 0 with two separate oxygen anti-bond against the valence electron of Yb in a TEB link, **(e)** fully bridged SiO_4 with two resonant bonds indicated by ellipses leading to four resonant 1.55 bond order Si-O interactions.

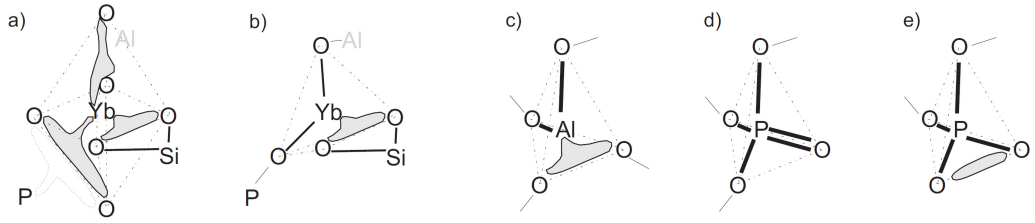

Fig. 2. **(a)** Six-fold coordinated Yb^{3+} with three (AlO_4, PO_6 and = Si<O_2 center) edge matches, **(b)** four-fold coordinated Yb^{3+} with one edge match = Si<O_2 center, **(c)** AlO_4 tetrahedron with four shared corners internally linked by two σ- and one TEB bond, **(d)** PO_4 tetrahedron with three shared corners and one double bond oxygen internally linked by four σ- and one π-bond, **(e)** PO_4 tetrahedron with two shared and two non-shared corners internally linked by four σ-bonds and the 5th electron in TEB (as in POHC of [17]).

The precursor state ii↑ with one polarized TEB↑ and no bond directly between the oxygen is shown in Fig. 1(c). A further precursor state 0 is in Fig. 1(d) shown for the part where two non-bridging oxygen (NBO) present anti-bond electrons to the valence electron of Yb in a polarized TEB↑. With respect to annealing both state ii and 0 is terminal as transitions among these hold no influence on absorption in the near infrared. As such they can be regarded as one state. The difference between state ii and 0 is of importance to which type of centers that may be regarded as precursors for PD – a discussion which is beyond the scope of this paper.

The fully bridged tetrahedral SiO_4 hold four Si-O bonds superimposed two resonant bonds (electron pair) as indicated by ellipses in Fig. 1(e). This resonance of double bonds results in 1.55 bond order for each Si-O interaction [14]. The PD process for the SiO_4 interface precursors may be sketched to initiate by exciting one Si to NBO interaction to ≈0.5 bond order [shown as ⋯ in Fig. 1] and hereby open the NBO for three-fold coordination (O≡) [15]. In a further excitation the NBO shifts host and forms state ii (= Si<O_2). State iii hold one Si to NBO interaction excited to ≈0.5 bond order such that a "½" bond forms in parallel to the polarized TEB link ("½+TEB"). For state II the second Si to NBO interaction is excited to ≈0.5 bond order and a σ-bond forms in parallel to the TEB link ("1+TEB"). This gives a 4 step process for the 0→ II transition in demand of 4 consecutive excitations.

The introduction of Yb^{3+} to corner shared SiO_4 tetrahedral networks is according to [16] as six-fold coordinated YbO_6. In Fig. 2(a) are the three valence electrons of Yb^{3+} represented by three TEBs (grey shaded areas) where each TEB is anti-bond against a pair of oxygen hereby leading to six-fold coordination in an octahedron. The D_3 symmetry with trigonal fields of YbO_6 leads to the $F_{7/2}$ and $F_{5/2}$ manifold splitting [16]. A trigonal field symmetry may, however, also be found in an YbO_4 tetrahedron comprising two σ - bond oxygen corners and one TEB linked edge as shown in Fig. 2(b). This as the field follows the bond axes of σ-bonds and is for the TEB given by the direction from the electron donor to the midpoint between the oxygen. This is taken to show that YbO_6 and YbO_4 are optically active in silica.

#187713 - $15.00 USD Received 25 Mar 2013; revised 7 May 2013; accepted 10 May 2013; published 17 May 2013

The introduction of Al^{3+} or P^{5+} to corner shared SiO_4 tetrahedral networks is as tetrahedral units. The AlO_4 shows in Fig. 2(c) four corners shared with the SiO_4 network by linking two corners with σ-bonds and two corners with a TEB bond. The PO_4 shows in Fig. 2(d) three corners shared with the SiO_4 network and its fourth corner terminated by double bond oxygen. The shared corners follow the structure of the SiO_4 network while the shared TEB edges of Yb or Al opens for the possibility of CC formation. Here the dynamic creation of CCs (by Yb inversion) is taken to rely on a direct link between Yb and the precursor as several studies [1,4,5] have shown – in that without the presence of Yb no CC formation is observed.

The number of shared TEB edges that may be matched by = Si<O_2 for each Yb^{3+} is 1 for YbO_4 (denoted by $\underline{\mathbf{Y}}O_2$) and 3 for YbO_6 (denoted by $|\underline{\mathbf{Y}}|$). Single Yb ions are incorporated into silica as YbO_4 and clusters of Yb and Al and/or P convert to YbO_6/AlO_6 for the central part with interface layer by either octahedral or tetrahedral ($YbO_4/AlO_4/PO_4$) coordination to the silica network. Here AlO_6 ($|\mathbf{A}|$) is the result of two Al-O to TEB conversions in going from Fig. 2(b) by adding one oxygen for each interaction and hereby reach Fig. 2(a). The PO_4 edge match P| is represented by the room temperature stable POHC structure of [17] in Fig. 2(e). Here the P = O double bond is converted to a TEB between the oxygen leaving the overall unit in neutral charge. The $\underline{Y}$ or $|\underline{Y}|$ share preferentially edge(s) (cluster) with other $\underline{Y}$, $|\underline{Y}|$, $\underline{A}$, $|\underline{A}|$, or P| in lowering the number of edges in need of coordination to the silica network.

Table 1. The Pauling ionic character of single bond interactions [19] and corresponding resonant TEB ionic character κ found as the geometric average of bonds where $\underline{\mathbf{Y}}O_2$ ($\underline{\mathbf{A}}O_2$) are edge connections between Yb (Al) and = Si<O_2 in tetrahedral units (Al is to share one corner with Yb). The $|\underline{\mathbf{Y}}|$/$|\underline{\mathbf{A}}|$ in octahedral units hold one edge connection to = Si<O_2 and two TEB linked edges to $\underline{\mathbf{Y}}$, $\underline{\mathbf{A}}$, $|\underline{\mathbf{Y}}|$, $|\underline{\mathbf{A}}|$ or P|.

Tetrahedral	$\underline{\mathbf{Y}}O_2$ / Yb-O		$\underline{\mathbf{A}}O_2$ / Al-O		Interaction	P-O	Yb-Yb	Yb-Al	Yb-P	Al-P
κ	0.746		0.567		κ	0.324	0	0.063	0.257	0.08
Octahedral	P|$\underline{\mathbf{Y}}$|P	P|$\underline{\mathbf{Y}}$|A	Y|$\underline{\mathbf{Y}}$|P	A|$\underline{\mathbf{Y}}$|A	Y|$\underline{\mathbf{Y}}$|A	Y|$\underline{\mathbf{Y}}$|Y	P|$\underline{\mathbf{A}}$|Y	Y|$\underline{\mathbf{A}}$|Y	A|$\underline{\mathbf{A}}$|Y	
κ	0.420	0.355	0.334	0.291	0.270	0.249	0.237	0.231	0.210	

In Table 1 the average ionic character of the TEBs within a tetrahedral or octahedral unit is given by the geometric average of the individual links. This is a consequence of the two states for each TEB which leads to formation of resonant spin paired TEB↓ to TEB↑ bonds for Yb|P, Yb|Al or Yb|Yb edge connections while the TEB to Si<O_2 (or its precursor) is "non-bond". The valence electrons of (Yb^{3+}, Al^{3+} or P^{5+}) is in Table 1 taken to form resonant bonds to their surroundings such that the valence electron density is influenced by the individual ionic character links. Here TEB↓ and TEB↑ are assumed to show identical ionic character.

3. The phonon and photon absorptions in = Si<O_2:·Yb

In the following the dissociation of bonds formed between oxygen of = Si<O_2:·Yb (state iii and II) by phonons and photons is described. An estimate for the bond energy is given in Eq. (1):

$$E_B = V_c(r,\kappa) + \kappa \cdot EA(O) - E_{IP}(\kappa), \tag{1}$$

where $V_c(r, \kappa)$ is the covalent bond energy (between oxygen in bond length r) added ionic character κ for the TEB in electron affinity to oxygen EA(O) = 1.479 eV [18] balanced by ionization potential $E_{IP}(\kappa) \approx \kappa \cdot E_X \cdot \exp(a_X \cdot (\kappa - 1))$ of X = Yb. Here $a_{Yb} = 0.157$ is found for ionization potential $E_{Yb} = 6.254$ eV [19] and $\kappa_{Yb\text{-}O} = 0.746$ [19]. This yields a TEB ionic character energy ($\kappa_{Yb\text{-}O} \cdot EA(O) - E_{IP}(\kappa_{Yb\text{-}O})$) in balance for $E_{ionic} = 1.02$ eV. The balanced ionic character energy for a TEB to Al is likewise determined to be 0.83 eV.

The covalent bond energy $V_c(r, \kappa)$ is a function of oxygen to oxygen bond length and the degree of polarization (ionic character κ) of the TEB link. This is a result of the "extra" electron charge partially shielding the oxygen to oxygen nuclei repulsion. Taken that covalent bond energy is additive and that a σ-bond on = Si<O_2 show a similar bond potential as single

#187713 - $15.00 USD Received 25 Mar 2013; revised 7 May 2013; accepted 10 May 2013; published 17 May 2013

σ-bond molecular O_2 ($c^1\Sigma_u^-$) and a 100% polarized bond of = Si<O_2^- show a similar bond potential as "1½" bond order superoxide O_2^- ($^4\Sigma_u^-$ and $^2\Pi_u$) the covalent bond energy $V_c(r, \kappa)$ of a σ-bond in parallel to a partially polarized TEB of ionic character κ is given by their interpolation. Here the covalent bond energy $V_b(r)$ from spectroscopic data of molecular oxygen [18] is fitted by the Morse potential function:

$$V_b(r) = D_E \cdot \left[\exp(-2a_\pm(r - r_0) - 2 \cdot \exp(-a_\pm(r - r_0)\right], \qquad (2)$$

where D_E is dissociation energy, r_0 the relaxed bond length and $a_\pm$ the potential well shape in a_+, $r > r_0$ and a_-, $r \le r_0$. The fitted parameters to [18] are given in Table 2.

The interpolated potential for κ degree of polarization is hereby given as:

$$V_c(r, \kappa) = V_\sigma(r) + \kappa \cdot E_{SZ}(r), \qquad E_{SZ}(r) = V_{\sigma+SZ}(r) - V_\sigma(r), \qquad (3)$$

where $V_\sigma(r)$ is the σ-bond ($c^1\Sigma_u^-$) potential by Eq. (2) and $E_{SZ}(r)$ is the shield set by potential difference $V_{\sigma+TEB\uparrow} - V_\sigma(r)$ and $V_{\sigma+TEB\downarrow} - V_\sigma(r)$ for a parallel TEB↑ and TEB↓, respectively.

Figure 3(a) shows the fitted 0% polarized σ-bond potential curve ($c^1\Sigma_u^-$) and 100% curves σ + TEB↑ ($^4\Sigma_u^-$) and σ + TEB↓ ($^2\Pi_u$) of superoxide as function of O to O bond length. Here the shields by the "extra" electron in TEB↑ increase and TEB↓ decrease the covalent σ-bond strength as found for the intermediate curves with Yb-O, Al-O and P-O interactions ionic character. Figure 3(b) shows the potential curves for "½" bond superoxide ($^2\Sigma_u^-$) (0%), "½ + TEB↓" ($C^3\Delta_u$) and "½ + TEB↑" ($A^3\Sigma_u^+$) molecular O_2 (100%) for fitted experimental data of [18] by parameters given in Table 2. The intermediate curves are derived by Eq. (3) and represent Yb-O, Al-O and P-O interactions ionic character. From Fig. 3(b) it is found that both TEB↑ and TEB↓ increase the bond strength for increasing degree of polarization. The covalent bond energy V_{Cx} for state x = (iii↓, iii↑, II↓, II↑) in parallel to TEB links of Table 1 are hereby determined and listed in Table 3. It is to be observed that the covalent bond energy for state II↑ is in the 1.14 eV – 1.37 eV range and for state II↓ in the 0.96 eV – 0.71 eV range while state iii↑ and iii↓ show covalent bond energies <0.86 eV even for full polarized TEBs.

Table 2. The potential energy for O-O bond, with spectroscopic term for molecular oxygen of [18] by: D_E dissociation energy, r_0 relaxed bond length and potential well shape parameters (a_- and a_+).

Bond		σ - bond	σ + TEB↑	σ + TEB↓	"½"	"½" + TEB↑	"½" + TEB↓
Spectroscopic term		$c^1\Sigma_u^-$	$^4\Sigma_u^-$	$^2\Pi_u$	$^2\Sigma_u^-$	$A^3\Sigma_u^+$	$C^3\Delta_u$
D_E	(eV)	1.065	1.502	0.616	0.090	0.860	0.775
r_0	(Å)	1.5174	1.63	1.63	1.75	1.5215	1.5260
a_- / a_+	($Å^{-1}$)	3.30 / 2.86	3.20 / 2.38	3.20 / 2.22	3.34 / 4.04	2.96 / 4.30	2.96 / 4.30

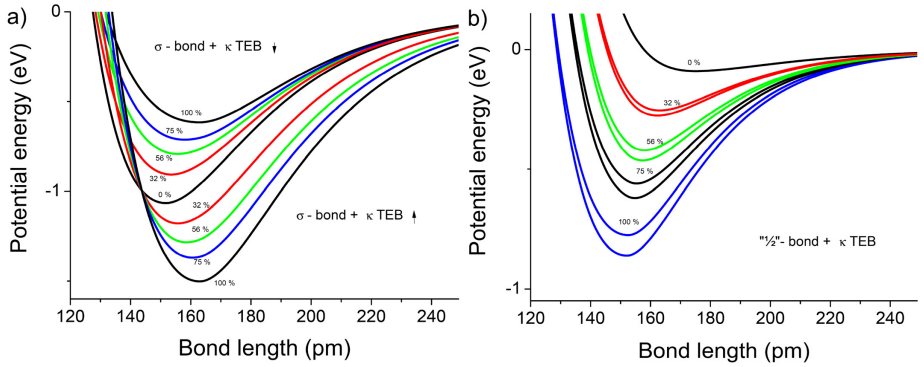

Fig. 3. **(a)** Potential bond energy as function of inter nuclei distance for single O-O sigma bond in parallel to (0 – 100% polarized) "½" (TEB↓ and TEB↑) bond, **(b)** Potential bond energy as function of inter nuclei distance for "½" bond in parallel to (0 – 100% polarized) "½" bond (TEB↓ and TEB↑).

#187713 - $15.00 USD Received 25 Mar 2013; revised 7 May 2013; accepted 10 May 2013; published 17 May 2013

Table 3. The = Si<O_2 (σ + TEB and ½ + TEB) covalent bond energy V_C (eV) for bond length (pm) in $\underline{X}O_2$ or $|\underline{X}|$ CC types for TEB ionic character κ gives the phonon transition energy. State II↑ ($E_{II\uparrow}$ (eV) by $\sigma_{II\uparrow}$ (eV) spread) and phonon assisted iii↑ ($E_{iii\uparrow}$ by $\sigma_{iii\uparrow}$) gives the bond to anti-bond photon excitation energy.

Type	κ	II↑				II↓		iii↑				iii↓	
		$V_{CII\uparrow}$	$r_{II\uparrow}$	$E_{II\uparrow}$	$\sigma_{II\uparrow}$	$V_{CII\downarrow}$	$r_{II\downarrow}$	$V_{Ciii\uparrow}$	$r_{iii\uparrow}$	$E_{iii\uparrow}$	$\sigma_{iii\uparrow}$	$V_{Ciii\downarrow}$	$r_{iii\downarrow}$
100%	1.000	1.502	163	2.07	-	0.616	163	0.860	152	1.76	-	0.775	153
$\underline{Y}O_2$	0.746	1.370	161	2.07	0.29	0.714	158	0.621	155	1.52	0.29	0.560	155
$\underline{A}O_2$	0.567	1.283	159	2.11	0.24	0.793	156	0.465	157	1.37	0.24	0.421	158
P|$\underline{Y}$|P	0.420	1.218	157	2.16	0.29	0.861	154	0.348	160	1.25	0.29	0.318	161
P|$\underline{Y}$|A	0.355	1.191	156	2.20	0.29	0.891	154	0.299	162	1.20	0.29	0.275	162
Y|$\underline{Y}$|P	0.334	1.182	156	2.21	0.29	0.901	153	0.284	162	1.18	0.29	0.262	163
A|$\underline{Y}$|A	0.291	1.165	155	2.24	0.29	0.922	153	0.254	163	1.15	0.29	0.235	164
Y|$\underline{Y}$|A	0.270	1.157	155	2.25	0.29	0.932	153	0.240	164	1.14	0.29	0.223	164
Y|$\underline{Y}$|Y	0.249	1.149	155	2.27	0.29	0.942	153	0.227	164	1.13	0.29	0.211	165
P|$\underline{A}$|Y	0.237	1.145	155	2.27	0.24	0.948	153	0.219	165	1.12	0.24	0.204	165
Y|$\underline{A}$|Y	0.231	1.142	155	2.28	0.24	0.951	153	0.215	165	1.12	0.24	0.201	166
A|$\underline{A}$|Y	0.210	1.135	154	2.29	0.24	0.961	153	0.202	166	1.10	0.24	0.189	166

Excitation of = Si<O_2:·Yb (state II or iii) by a phonon will dissociate the bond between oxygen for phonon energy in excess of the covalent bond energy of Eq. (1). This excitation is without change to the resonant TEB ionic character.

For an incoming photon electric field vector **E** of angular frequency ω will the dipole moment **μ** of the = Si<O_2:·Yb interaction initiates a torque on TEB↑ (force in opposite directions for Yb and the TEB↑ electron). For TEB↓ either of the anti-bond electrons ↑ (of O) initiates an elastic ↑↓ torque exchange with the bond ↓ electron (of Yb) which is without absorption of energy. The torque on TEB↑ does temporary increase the degree of ionization of Yb with perturbation given by the energy V(t) as function of time t in Eq. (4):

$$V(t) = \mu \cdot E \cdot \exp(i\omega \cdot t), \tag{4}$$

where the dipole strength $|\boldsymbol{\mu}|^2 = |\int \psi_{TEB}(\mathbf{r})\ \boldsymbol{\mu}\ \psi_{TEB*}(\mathbf{r})d\mathbf{r}|^2$ with $\psi_{TEB}(\mathbf{r})$ and $\psi_{TEB*}(\mathbf{r})$ wave functions for the relaxed and distorted TEB electron field, respectively. The torque leads to absorption of the electric field for invariant O to O bond length in σ→ σ* (bond to anti-bond) excitation for photon energy in excess of:

$$E_{II\uparrow} = V_{b*}(r_{II\uparrow}) - V_b(r_{II\uparrow}) - \kappa \cdot E_{SZ}(r_{II\uparrow}), \tag{5}$$

where $V_{b*}(r_{II\uparrow})$ is the σ*-bond potential and $V_b(r_{II\uparrow})$ the σ-bond potential for CC bond length r_{II} with $E_{SZ}(r_{II\uparrow})$ shields as given by Eq. (3). The anti-bond $V_{b*}(r_{II\uparrow})$ is $R_*(\kappa,T)$ more anti-bonding than the σ-bond as result of the low electron density between the nuclei:

$$V_{b*}(r_{II\uparrow}) = (1 + R_*(\kappa,T)) \cdot D_E \cdot \left[\exp(-2a_{\pm}(r_{II\uparrow} - r_0)\right], \tag{6}$$

where D_E is dissociation energy, r_0 the relaxed bond length and $a_{\pm}$ the potential well shape in a_+, $r > r_0$ and a_-, $r \le r_0$ as specified for the σ-bond in Table 2. The $R_*(\kappa,T)$ is given by the "missing" electron density (relative to a free atom) between the nuclei R_* that partly is interfered by the κ ionic character TEB electron $(1-\kappa \cdot R_*)$ and by phonon interference on the charge distribution ($\delta R_* \cdot T$) – both adding electron density between the nuclei. The relative (decrease) to the anti-bond increase as function of κ and T is hereby:

#187713 - $15.00 USD Received 25 Mar 2013; revised 7 May 2013; accepted 10 May 2013; published 17 May 2013

$$R_*(\kappa,T)=\left[1-\kappa\cdot R_*\right]\cdot(R_*-\delta R_*\cdot T),\qquad(7)$$

where the experimental data of section 4 are fitted by $R_* = 0.58$ and $\delta R_* = 10^{-3}$ K^{-1}.

The CC absorption $E_{II\uparrow}$ at room temperature is derived by insertion of Eq. (6) and (7) into Eq. (5) as given in Table 3 for the TEB sites of Table 1. Increase (decrease) in temperature will linearly shift the absorption center to lower (higher) center energy. The spread to the $\sigma\rightarrow\sigma^*$ excitation absorption $\sigma_{II\uparrow}$ is set by the TEB ionic character energy of the Yb-O and Al-O interactions. Here the ionic character perturbation during photon excitation opens for ionic character energy to add or subtract the excitation as kinetic (+) or potential (–) energy released by the Yb-O or Al-O interactions. Taken the spread in ionic character energy to represent 3.5 standard deviations (>99.95%) of a Gaussian distribution $\sigma_{II} = E_{ionic}/3.5$ the spread for TEBs to Yb is 1.02 eV/3.5 = 0.29 eV and to Al is 0.83 eV/3.5 = 0.237 eV as given in Table 3.

For state iii$\uparrow$ the "½" bond (TEB$\downarrow$) excitation to anti-bond (TEB$\uparrow$) require excitation of a 1.55 to ≈0.5 bond order Si-O interaction along with a spin flip. This TEB$\downarrow$ + TEB$\uparrow\rightarrow$ TEB$\uparrow$ + TEB$\uparrow$ transition demands collaboration of a phonon why it is taken to show insignificant optical absorption for the $E_{iii\uparrow}$ transitions given in Table 3 at room temperature. Strain to the material or increase in temperature may, however, lead to that the photon absorption become observable but for the present model this is not included.

For both state iii and II the TEB dipole initiate an excitation transfer to the ≈0.5 bond order Si to ≡O interaction dipole. According to [15] neutral ≡O in Si to O interactions hold doublet-to-doublet transitions at 2.7 eV and 2.9 eV with oscillator strengths of $\approx10^{-1}$ and another at 4.4 eV with oscillator strength of $\approx10^{-3}$. This neutral ≡O (of three Si-O interactions) hold a single electron in (doublet) ground state which may be excited to either of the doublet states. In the present context the ≡O center is surrounded by a Si-O (⋯), an O-O (either σ- or ½-bond) and a TEB to Yb interaction which reduces the electron density of the TEB to Yb interaction relative to the Si-O (⋯) interactions in [15]. The reduced electron density (increase in localization of a hole) is taken to down-shift the optical absorption energy in proportion to the ionic character of the TEB in analogy to what is found for self-trapped holes in [20]. The experimental absorption spectra of section 5 are matched by applying:

$$E_{\equiv}(\kappa)=2.98-0.6\cdot\kappa\qquad(8)$$

The parameter choice in Eq. (8) yields 2.7 eV in peak absorption for a Si-O interaction ionic character [19]. It is further taken that all ≡O centers show spread identical to state II: $\sigma_{\equiv O} = \sigma_{II\uparrow}$ as both excitations are by dipole-to-dipole excitation transfer from the TEB dipole.

For state 0 the precursor is not expected to result in absorption in the visible or near infrared while state ii, iii and II may show additional centers created in parallel to = Si<O_2 during the PD process. The ODC(II) hold ≈5 eV and 3.15 eV absorption where the latter show $1.6\cdot10^{-7}$ in absorption strength [5] which is several orders of magnitude below the in [15] estimated absorption strength of neutral ≡O. Further may Al (≈2.9 eV [20]) and P (≈3.1 eV, ≈2.5 eV and ≈2.2 eV [17]) contribute with oxygen hole centers. However, taken the dispute on the actual nature of the PD process such additional centers are not included.

The absorption is hereby due to PD generated CCs (state II$\uparrow$) and ≡O (state II$\uparrow$ with two ≡O and state iii$\uparrow$ with one ≡O) for photon frequency ν taken to be proportional to the dipole strength (TEB ionic character κ_z) in the sum over all CC sites given by Eq. (9):

$$\alpha(\nu)=\sum_z\kappa_z\cdot\rho(z)\cdot\left(\sigma_{a,\equiv}\cdot g_{\equiv}(\nu,\kappa_z)\cdot(N_{iii\uparrow}+2N_{II\uparrow})+\sigma_{a,\uparrow}\cdot g_{II\uparrow}(\nu,\kappa_z)\cdot N_{II\uparrow}\right),\qquad(9)$$

where κ_z is the TEB average ionic character of CC site type z (as given in Table 3) with ρ(z) distribution of CC site type z (where Σ ρ(z) = 1), $\sigma_{a,\equiv}$ and $\sigma_{a,\uparrow}$ are the absorption cross section

#187713 - $15.00 USD Received 25 Mar 2013; revised 7 May 2013; accepted 10 May 2013; published 17 May 2013

of the TEB↑ to σ→ σ* and ≡O electronic excitations, $N_{iii\uparrow}$ and $N_{II\uparrow}$ the population number in state iii↑ and II↑ while $g_{\equiv}(\nu, \kappa_z)$ and $g_{II\uparrow}(\nu, \kappa_z)$ are given by Eq. (10):

$$g_X(\nu,\kappa_z) = \exp(-½\cdot\left[\frac{h\nu - E_X(\kappa_z)}{\sigma_X(\kappa_z)}\right]^2), \tag{10}$$

where $E_{\equiv}(\kappa_z)$ is given by Eq. (8) and $\sigma_{\equiv}(\kappa_z) = \sigma_{II\uparrow}(\kappa_z)$, while $\sigma_{II\uparrow}(\kappa_z)$ and $E_{II\uparrow}(\kappa_z)$ are given in Table 3 for CC type z and h is the Planck's constant.

4. Markov chain description of PD color center anneal

The annealing of pre-darkened material is in this section described by a Markov chain for the different bonds of section 2 and 3 with phonon activated state transitions by displacive transitions of 4-member SiO_4 rings carrying the CC precursor as proposed in [2].

The CCs (state II) hold two three-fold coordinated oxygen (≡O) in = Si<O_2 as shown in Fig. 1(a). The ≡O is in [15] found to hold ≤20% weaker Si-O bonds than regular Si-O bonds (444 kJ/mol or 4.6 eV/bond [21]) of pure silicon dioxide giving $E_{\equiv}$ ≈0.9 eV for its formation. The transition from state ii (with two ordinary Si-O bonds) to state II (with two ≡O) is through state iii (with one ≡O) as shown in Fig. 4. State iii↓ hold a "½" bond (TEB↓) in parallel to TEB↓ while state iii↑ is a "½" bond in parallel to TEB↑. Here ii→ iii transitions is by ≡O generation in overcoming O to O repulsion (≈0.78 eV and ≈0.86 eV as found in Table 3) for activation energy $E_{\equiv 1}$ and $E_{\equiv 3}$, respectively, as given in Table 4. The ii→ 0 is by E_{DT} = 1.53 eV [2] in a displacive transition that facilitate the oxygen transfer. As $E_{\equiv 3} > E_{\equiv 1} > E_{DT}$ both state ii and 0 are terminal with respect to annealing (when monitored by ≈600 nm absorption).

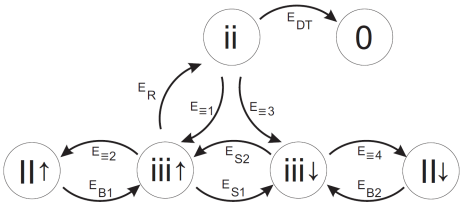

Fig. 4. State diagram for annealing of PD material with activation energies for transitions, note E_{B1} is II↑ and E_{B2} is II↓ covalent bond energy of Table 3 for the respective CC site ionic character.

Bond state iii↑ (½ + TEB↑)→ (non-bond) ii is by excitation (E_R) through ½ (TEB↓) bond to anti-bond (TEB↑) spin flip to the bond electron. For state iii↓ this process results in iii↓→ iii↑ (E_{S2}) as the TEB↓ of the link shifts orbit with TEB↑ (lowest potential energy). The iii↑→ iii↓ transition is by dissociation and spin flip (E_{S1}) to the bond electron. The iii↓→ II↓ and iii↑→ II↑ is by ≡O generation and bond exchange. Here both bonds gain potential energy for activation energies ($E_{\equiv 2}$ and $E_{\equiv 4}$) by ≡O generation. The II↑→ iii↑ (E_{B1}) and II↓→ iii↓ (E_{B2}) follows on "1" bond dissociation by phonon activation E_{B1} and E_{B2} followed by "½" bond reformation. The parameters applied for the various activations energies are given in Table 4 in actual values as found by best fits to the experimental data.

Table 4. Transition activation energies

E_{DT}	E_R	E_{S1}	E_{S2}	E_{B1}	E_{B2}	$E_{\equiv} = E_{\equiv 2} = E_{\equiv 4}$	$E_{\equiv 1}$	$E_{\equiv 3}$
1.53 eV	0.98 eV	0.84 eV	0.86 eV	Table 3	Table 3	0.9 eV	1.68 eV	1.76 eV

The phonon activation of CC sites is given by the heat dissipated in a unit volume of fiber core. The phonons are carried by SiO_4 rings ("fixated" gas molecules) with expected number density of phonons of energy E given by the Bose-Einstein distribution $[\exp(E/(k_B T)) - 1]^{-1}$.

#187713 - $15.00 USD Received 25 Mar 2013; revised 7 May 2013; accepted 10 May 2013; published 17 May 2013

Here k_B is Boltzmann constant and T fiber core absolute temperature. From Avogadros number, atomic masses [16] and ≈2.2 g/cm^3 mass density the silica hold $6.61\cdot10^{22}$ cm^{-3} atoms. With each SiO_2 ring element to bring 2 atoms to the ring and to hold 2 degree of freedom for average 6-member rings the total number of rings is $N_T \approx 1.1\cdot10^{22}$ cm^{-3}. The number of CC sites N_S is given by the method of manufacture and it is assumed that all sites are on 4-member planar rings in a relative small number compared to the total ring population N_T. The 4-member planar rings hold an inscribed diameter Λ of ≈3 Å in SiO_4 units of 2.65 Å between edge oxygen. This leads for speed of sound in fused silica $v_s \approx 5980$ m/s to a phonon "collision" frequency for the 4-member rings of $\nu_0 = v_s/\Lambda \approx 20$ THz.

The CC sites of ionic character z given in Table 3 are distributed by ρ(*z*) with $\rho(z)\cdot N_S$ rings to carry CC type z. Each of the CC sites is in either of the states U = (0, ii, iii↓, iii↑, II↓, II↑) to time t where $\rho(z)\cdot N_S = \Sigma N_{U,z}(t)$ when summed over all states. The probability for a randomly chosen ring to hold CC site z in state U is hereby $N_{U,z}(t)/N_T$. This leads to the rate of phonons with activation energy $E_{U,Z}$ in rings carrying a CC site type z in state U by Eq. (11):

$$k_{U,z}(T,t) = \frac{N_{U,z}(t)}{N_T}\cdot\nu_0\cdot\left[\exp(\frac{E_{U,z}}{k_B\cdot T})-1\right]^{-1} \tag{11}$$

The process of state transition by phonon activation energy $E_{U,z}$ for a CC site type z in state U is given by the single element reaction:

$$-\frac{dN_{U,z}(t)}{dt} = k_{U,z}(T,t)\cdot N_{U,z}(t) \Leftrightarrow -\Delta N_{U,z}(t) = (1-\exp(-k_{U,z}(T,t)\cdot\Delta t))\cdot N_{U,z}(t), \tag{12}$$

where dN/dt ≈ΔN/Δt and Taylor expansion (ε = 1-(1-ε) ≈1 – exp(-ε) for ε << 1) is applied in Eq. (12) for division of time into Δt transition steps.

For CC site type z the transitions of the Markov chain hold several transition routes as shown in Fig. 4 why change rate for state U is a sum of rates $k_U(T,t) = \Sigma k_j(T,t)$. This results in $\exp[-\Sigma k_j(T,t)\cdot\Delta t]$ decrease in state U population and $k_j(T,t)/\Sigma k_j(T,t)\cdot(1-\exp[-\Sigma k_j(T,t)\cdot\Delta t])$ increase in state j population with activation energy E_j in the U→ j transition. As there is no return path from terminal state 0 the transitions are handled in the 6x5 Markov matrix $\underline{\underline{M}}_Z$:

$$\underline{\underline{M}}_Z = \begin{pmatrix} A_1\cdot k_{DT}(T,t)/k_{\Sigma1} & 0 & 0 & 0 & 0 \\ 1-A_1 & 0 & A_3\cdot k_R(T,t)/k_{\Sigma3} & 0 & 0 \\ A_1\cdot k_{\equiv3}(T,t)/k_{\Sigma1} & 1-A_2 & A_3\cdot k_{S1}(T,t)/k_{\Sigma3} & A_4 & 0 \\ A_1\cdot k_{\equiv1}(T,t)/k_{\Sigma1} & A_2\cdot k_{S2}(T,t)/k_{\Sigma2} & 1-A_3 & 0 & A_5 \\ 0 & A_2\cdot k_{\equiv4}(T,t)/k_{\Sigma2} & 0 & 1-A_4 & 0 \\ 0 & 0 & A_3\cdot k_{\equiv2}(T,t)/k_{\Sigma3} & 0 & 1-A_5 \end{pmatrix}, \tag{13}$$

where $A_j = [1-\exp(-k_{\Sigma j}\cdot\Delta t)]$ for j = [1,5] and $k_{\Sigma1} = k_{DT}(T,t) + k_{\equiv3}(T,t) + k_{\equiv1}(T,t)$, $k_{\Sigma2} = k_{S2}(T,t) + k_{\equiv4}(T,t)$, $k_{\Sigma3} = k_R(T,t) + k_{S1}(T,t) + k_{\equiv2}(T,t)$, $k_{\Sigma4} = k_{B2}(T,t)$ and $k_{\Sigma5} = k_{B1}(T,t)$ in Eq. (13) are for the PD process of CCs type z in TEB ionic character.

For each CC site population z vectors $\mathbf{p_{z,1}} = (N_0, N_{ii}, N_{iii\downarrow}, N_{iii\uparrow}, N_{II\downarrow}, N_{II\uparrow})$ and $\mathbf{p_{z,2}}$ contains the populations before and after the transition in time step Δt for the matrix multiplication:

$$\overrightarrow{p_{z,2}} = \underline{\underline{M}}_Z * \overrightarrow{p_{z,1}} \tag{14}$$

The rate coefficients for the matrix multiplication of Eq. (14) are recalculated after each time step as the concentration changes for the various states. The absorption as function of time is determined by the $N_{iii\uparrow,z}$ and $N_{II\uparrow,z}$ populations by insertion into Eq. (9).

#187713 - $15.00 USD Received 25 Mar 2013; revised 7 May 2013; accepted 10 May 2013; published 17 May 2013

5. Annealing of pre-photo darkened material

In this section the kinetic model for annealing of PD material is applied on experimental data from thermal cycles [11], thermal ramps [12] and isothermal anneals [13].

In [11] a short section of pre-darkened commercial 20 μm core diameter large mode area (LMA) fiber is subjected to temperature cycles with 60–180 K/min heating/cooling rates. Absorption data measured at 600 nm [from Fig. 2 and Fig. 1(b) in [11]] are given by solid and open dots in Fig. 5. These are from two experiments on the same fiber (F1) with PD at identical conditions. The solid dots are for a 296 K→ 598 K→ 296 K→ 700 K (→ 296 K) cycle and the open dots are a 296 K→ 905 K → 296 K cycle. The core material is not specified except by ≈0.5 dB/m pump absorption at 915 nm [11] which suggest 0.15 mol % Yb_2O_3 by Al_2O_3 co-doping and yield $N_{Yb} = 6.5 \cdot 10^{19}$ cm^{-3} for evenly distributed Yb ions.

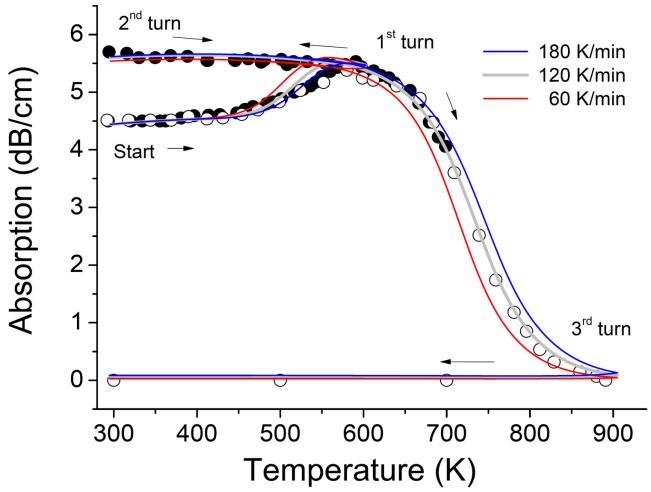

Fig. 5. Experimental temperature cycles (dots) from [11] with model (solid lines) anneal of pre-darkened fiber at 60-180 K/min rates for CC type/ state distribution as given in Table 5.

Table 5. The fiber F1 distribution on $\underline{X}O_2$ and $|\underline{X}|$ CCs of ionic character κ, number of active sites relative to number of Yb (N_{AS}/N_{Yb}) and initial distribution of tetrahedral and octahedral CCs on states (II and iii).

CC	$\underline{Y}O_2$	$\underline{A}O_2$	$A\|\underline{Y}\|A$	$Y\|\underline{Y}\|A$	$Y\|\underline{Y}\|Y$	$Y\|\underline{A}\|Y$	$A\|\underline{A}\|Y$	N_{AS} / N_{Yb}
κ	0.746	0.567	0.291	0.270	0.249	0.231	0.210	1.0%
ρ(CC)	53%	5%	14%	-	-	-	28%	

Initial state	$\underline{Y}O_2$ & $\underline{A}O_2$	II↑:	66%	II↓:	22%	iii↑:	6%	iii↓:	6%
distribution	$A\|\underline{Y}\|A$ & $A\|\underline{A}\|Y$	II↑:	97%	II↓:	1%	iii↑:	1%	iii↓:	1%

In [2] it is proposed that there is a direct link between number of = $Si<O_2$ sites and ODC(II) which combined with the linear relation of [1] yields $N_{AS} = 0.01 \cdot N_{Yb}$ for Yb/Al material. Here N_{AS} is the number of active CC sites – i.e. $N_{AS} = N_{iii\downarrow} + N_{iii\uparrow} + N_{II\downarrow} + N_{II\uparrow}$. For the Markov chain model description of annealing of pre-darkened material, however, $N_S \approx N_{AS}$ as the CC sites in terminal states (ii and 0) remain here during annealing.

#187713 - $15.00 USD Received 25 Mar 2013; revised 7 May 2013; accepted 10 May 2013; published 17 May 2013

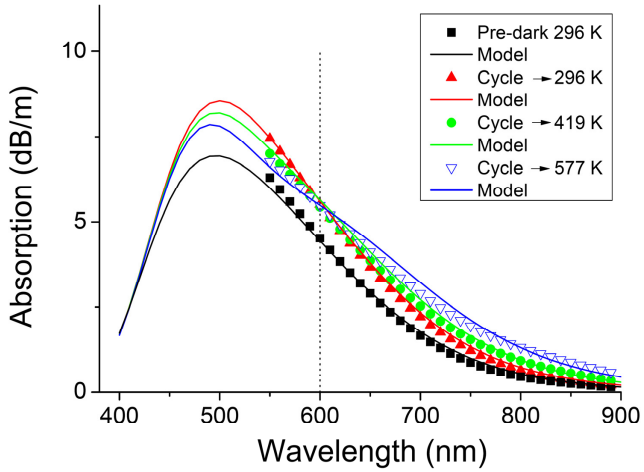

Fig. 6. Experimental absorption spectra (dots) from [11] with (solid curves) model anneal of pre-darkened fiber F1. The measures are after PD at 296 K and after a 296K→ 598K→ 296K thermal cycle and further →419 K and →577 K.

This leads for fiber F1 to the absorption cross sections $\sigma_{a,\equiv} = \sigma_{a,\uparrow} = 303$ pm^2. Here it is noted that a uniform reduction in either cross section or N_{AS} followed by a corresponding increase in the other will yield equal results. As there in addition is no model available for the distribution of Yb and Al atoms on tetrahedral and octahedral sites this is done by trial and error as given in Table 5. Here shift among nearby ionic character CCs lead only to small changes in the overall form of the anneal ramp curve why the distribution in Table 5 present only a rough estimate. However, for this choice of distribution and absorption cross sections the solid lines in Fig. 5 are found.

The thermally induced increase in absorption of Fig. 5 is met by ≈70% of the tetrahedral CCs in state II↑ and ≈30% distributed to II↓, iii↓ and iii↑ while nearly all octahedral CCs are in II↑. The annealing cycles of Fig. 5 are calculated for 60, 120 and 180 K/min rates with the best overall fit for 120 K/min.

In Fig. 6 the spectral distribution in the 550 nm to 900 nm range is shown for the pre-darkened fiber F1 at 296 K and after thermal cycle 296 K→ 598 K→ 296 K and further to 419 K and 577 K as indicated by the dots [from Fig. 3 in [11]]. The spectra are in [11] found to show no change in absorption at 612 nm upon the annealing cycle in the further increase in temperature from 296 K to 577 K. The state model finds no such spectral pivot point but the spectral shifts meet a region of low variation in absorption around 600 nm identified by the dotted line in Fig. 6. The spectral shape for temperatures <450 K is independent on ramp rate while for >450 K it shows dependence on ramp rate. I.e. if it takes more than ≈1 min to obtain the spectrum at 577 K the recorded form is skewed in relation to its "true" spectral form.

The model predicts that at 120 K/min rate a 598 K → 296 K→ 598 K temperature cycling of fiber F1 result in unchanged number of state II and iii population. This leads to that either is the observed spectral shift in Fig. 6 (< 450 K) a result of thermally induced change in full width half maximum (FWHM) of the absorption cross section [11], temperature dependent absorption cross sections [12] or as here applied a temperature dependent anti-bond level $R_*(\kappa,T)$ as given by Eq. (7). The latter $R_*(\kappa,T)$ results in linear shift to CC peak absorption for unchanged peak absorption cross section.

In [12] are short sections of pre-darkened fibers (F2) of 0.6 mol % Yb_2O_3, 3.9 mol % Al_2O_3 and 0.6 mol% P_2O_5 core composition subjected to 5 – 20 K/min ramp rates. The absorption data [Fig. 3(a) in [12]] measured at 633 nm is shown in Fig. 7 as dots. The solid lines in Fig. 7 are for a CC type distribution on octahedral CCs where nearly all are in state II↑ for the pre-darkened fiber as given in Table 6. By applying identical absorption cross

#187713 - $15.00 USD Received 25 Mar 2013; revised 7 May 2013; accepted 10 May 2013; published 17 May 2013

sections as for F1 the absorption level of Fig. 6 suggest that $N_{AS} = 0.0069 \cdot N_{Yb}$ or that F2 performs ≈45% better than the Yb/Al material of F1 with respect to PD induced absorption per Yb ion.

Table 6. The fiber F2 distribution on $\underline{X}O_2$ and $|\underline{X}|$ CCs of ionic character κ, number of active CC sites relative to number of Yb (N_S/N_{Yb}) and initial distribution on states (II and iii) for octahedral CCs.

CC	$\underline{Y}O_2$	$\underline{A}O_2$	$\|P\|\underline{Y}\|P\|$	$\|P\|\underline{Y}\|A$	$A\|\underline{Y}\|A$	$\|P\|\underline{A}\|Y$	$A\|\underline{A}\|Y$	N_{AS} / N_{Yb}
K	0.746	0.567	0.420	0.355	0.291	0.237	0.210	0.69%
ρ(z)	-	-	23%	-	-	77%	-	
Initial state distribution			II↑: 97%	II↓: 1%		iii↑: 1%	iii↓: 1%	

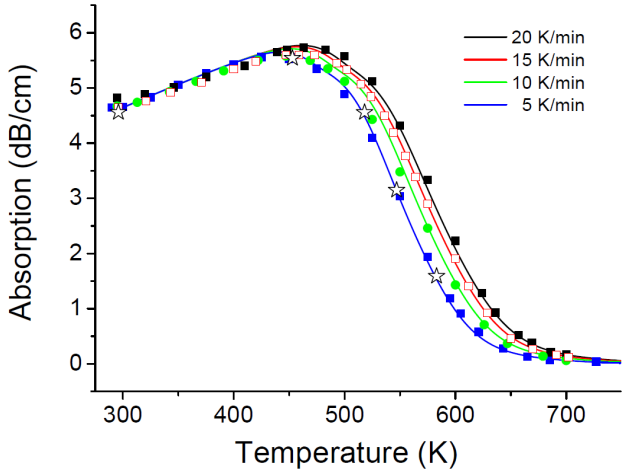

Fig. 7. Experimental temperature ramps (dots) from [12] with model anneal of pre-darkened fiber F2 at 5 – 20 K/min rates for CC type/ state distribution of Table 6.

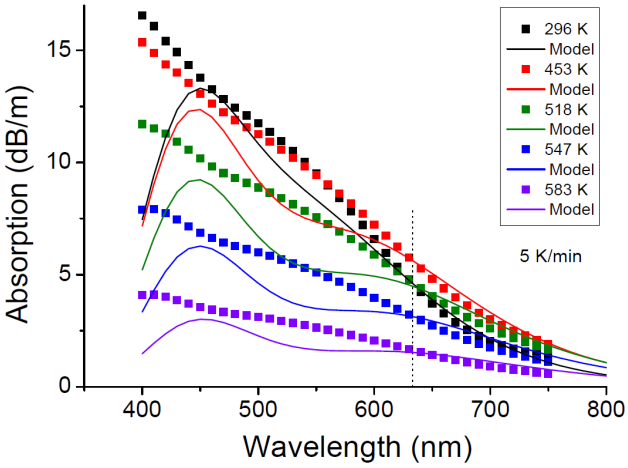

Fig. 8. Experimental absorption spectra (dots) from [12] with (solid curves) model anneal of pre-darkened fiber F2. The measures are for pre-darkened fiber at 296 K and after ramp to 453 K, 518 K, 547 K and 583 K for 5 K/min ramps.

In [22] it is proposed that Al and P form salvation shells to Yb and it is found that P in contrast to Al distribute evenly within the silica matrix. This fits the N_{AS} applied for F1 and F2 if P offers nucleation sites for Yb that replaces tetrahedral and Al dominated octahedral CCs. The absorption between 400 nm and 750 nm [from Fig. 2 of [12]] is shown in Fig. 8 by

#187713 - $15.00 USD Received 25 Mar 2013; revised 7 May 2013; accepted 10 May 2013; published 17 May 2013

dots for the F2 fiber pre-darkened at 296 K and annealed at 453 K, 518 K, 547 K and 583 K. In [12] the thermal history of the spectra is not specified but the 633 nm absorption (identified by the dotted line) find a good fit to 5 K/min ramps as indicated in Fig. 7 by stars. The solid lines in Fig. 8 are for 5 K/min rates found to give good match to the spectra above ≈600 nm while "missing" parts can be observed at shorter wavelengths. These "missing" parts correspond for the presently applied parameters for ≡O absorption in Eq. (8) to a center with peak absorption near ≈400 nm (3.1 eV) and another near ≈540 nm (2.3 eV). Here the ≈2.3 eV peak absorption and strength is directly influenced by choice of ≡O parameters. However, the "missing" parts could be due to phosphorous oxygen hole-center absorption at ≈3.1 eV, 2.5 eV and 2.2 eV [17] that follows the CC formation and bleaching. Here ≈3.1 eV absorption decreases in strength with annealing while ≈2.3 eV absorption first grows up to ≈518 K and then decreases for higher temperatures. This difference may be due to that part of the ≈3 eV absorption is from the second doublet-to-doublet transitions of ≡O which for a Si-O interaction would lead to ≈2.9 eV absorption. This second transition is, however, not included in the present model.

Table 7. Fiber F3 distribution on $\underline{\mathbf{X}}O_2$ and $|\underline{\mathbf{X}}|$ CCs of ionic character κ, number of active CC sites relative to number of sites in F1 and initial distribution on states (II and iii) for tetrahedral and octahedral CCs.

CC	$\underline{\mathbf{Y}}O_2$	$\underline{\mathbf{A}}O_2$	A|$\underline{\mathbf{Y}}$|A	Y|$\underline{\mathbf{Y}}$|A	Y|$\underline{\mathbf{Y}}$|Y	Y|$\underline{\mathbf{A}}$|Y	A|$\underline{\mathbf{A}}$|Y	N_{AS}
κ	0.746	0.567	0.291	0.270	0.249	0.231	0.210	"7.3· F1"
ρ(z)	3%	20%	26%	-	-	-	51%	

Initial state distribution										
$\underline{\mathbf{Y}}O_2$ & $\underline{\mathbf{A}}O_2$	II↑:	58%	II↓:	30%	iii↑:	6%	iii↓:	6%
A|$\underline{\mathbf{Y}}$|A & A|$\underline{\mathbf{A}}$|Y	II↑:	97%	II↓:	1%	iii↑:	1%	iii↓:	1%

In [13] three isothermal anneals on the same pre-darkened 20 μm alumino-silicate ytterbium doped LMA fiber (F3) are fitted by $\Delta\alpha_n = [1 + (t/\tau)^{\beta}]^{-1}$. The dots in Fig. 9 represent these fits scaled to 1750 dB/m (as specified in Table 1 of [13]). The core material composition is not presented in [13] but by applying identical CC absorption cross sections as for F1 (and F2) the number of CC sites is fitted by ≈7.3 times the number of sites in F1. The distribution on CC type and states in Table 7 is found by match to the temporal data for the 556 K anneal [from Fig. 7 of [23]] shown as open dots in Fig. 10. The solid dots in Fig. 10 are from the [13] fits. The annealing in Fig. 10 is by the shown temperature profile where identical ramps are applied for the 510 K and 676 K anneals of Fig. 9.

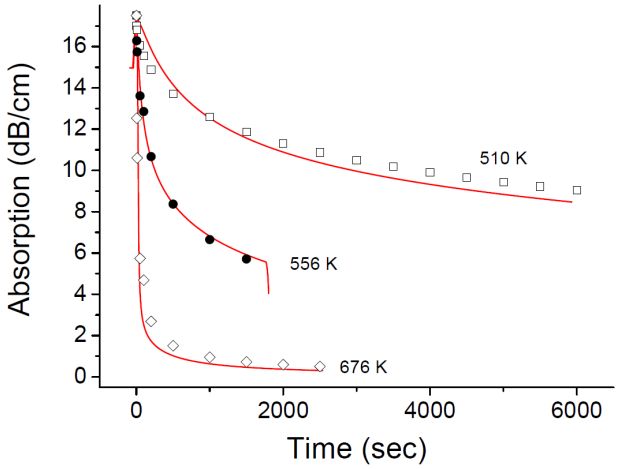

Fig. 9. Absorption as function of time for isothermal anneals at 510 K, 556 K and 676 K with dots from [13] with solid curve model calculations for F3 by CC type and state distribution as given in Table 7.

#187713 - $15.00 USD Received 25 Mar 2013; revised 7 May 2013; accepted 10 May 2013; published 17 May 2013

The initial increase in absorption for 296 K→ 556 K in Fig. 10 is met by 58% tetrahedral CC population in state II↑ and 42% in state II↓, iii↑ and iii↓ for the pre-darkened fiber. This distribution is applied for all isothermal anneals of F3. The actual performance of the F3 fiber is due to missing data on the level of Yb ion doping in the material not possible to assess.

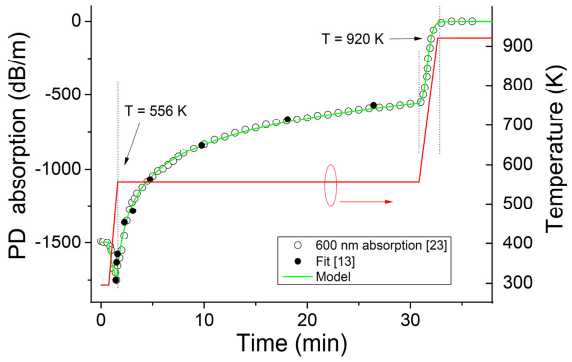

Fig. 10. Absorption as function of time for 296 K→ 556 K ramp, 556 K anneal and 556K→ 920 K ramp given by open dots from [23], solid dots from [13] and with model solid curve for F3 by CC type and state distribution as given in Table 7.

In [13] demarcation energy $E_D = k_B T \ln(\nu_D t)$ is applied to convert the time t of isothermal anneals into an energy scale. For constant characteristic frequency ν_D it is assumed that the trap release is by a 1st order reaction with rate $k = \nu_D \cdot \exp(-E_A/k_B T)$ for activation energy E_A. After time t at temperature T the fiber holds 1/e of the population trapped so $k \cdot t = 1$ divides the population by demarcation energy E_D in that for $E_A \le E_D$ the traps are open and for $E_A > E_D$ the traps are closed. The absorption data as function of time is hereby transformed into a cumulative distribution of trap activation energy which brings the data of isothermal anneals onto a single curve. This may be observed in [13] by leaving out the initial values of the highest annealing temperatures. The first derivative of the curve $d(\Delta\alpha)/dE_D$ is then the probability frequency for the trap release.

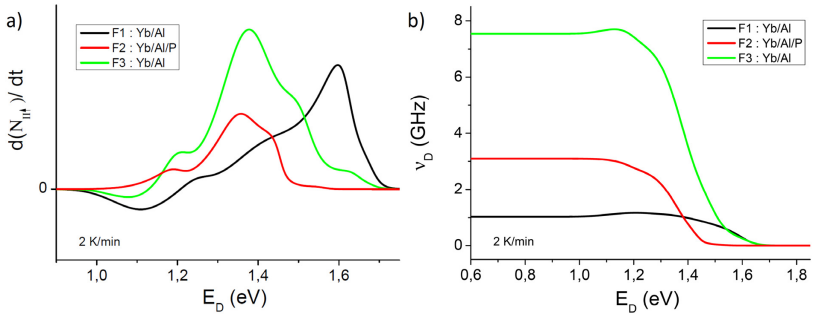

Fig. 11. **(a)** Probability frequency as function of demarcation energy E_D for pre-darkened fibers F1, F2 and F3 by 2 K/min anneal ramps by induced loss at 1000 nm, and hereto corresponding **(b)** characteristic frequency ν_D as function of demarcation energy E_D

For the present state model the E_D technique is still applicable even though the reaction rate is concentration dependent and hereby of 2nd order. For the loss induced at 1000 nm only state II↑ is taken to induce absorption so the characteristic frequency depends here on time as: $\nu_D = \Sigma N_{II\uparrow,z}(t) \cdot \nu_0/N_T$, where $\Sigma N_{II\uparrow}(t)$ is the population in state II↑ summed over all CC sites. In Fig. 11(a) is the probability frequency $d[N_{II\uparrow}(t)]/dE_D$ shown against E_D for F1, F2 and F3 fiber anneals by 2 K/min ramps based on the induced absorption at 1000 nm. The corresponding characteristic frequency ν_D as function of E_D is shown in Fig. 11(b). This brings the activation energy for F1, F2 and F3 on a common scale.

#187713 - $15.00 USD Received 25 Mar 2013; revised 7 May 2013; accepted 10 May 2013; published 17 May 2013

It is for the E_D technique to be observed that if absorption of the individual CC types scale with average ionic character the activation energy determined from number of sites will not in all cases agree with the value found directly from absorption. Here mixed tetrahedral and octahedral sites show larger difference between the estimates based on number of sites and absorption which makes it difficult to exactly relate a measured isothermal or ramp anneal profile to activation energy. It is further to be noted that the choice of absorption cross sections influences the values for activation energy in that a change in number of CC sites lead to change in the characteristic frequency.

The E_D analysis in [13] for fiber F3 gives 1.32 eV in activation energy with 0.31 eV in FWHM by static ν_D = 2 GHz. For the present state model with a dynamic ν_D and from the number of sites the F3 fiber is found to exhibit peak activation energy at ≈1.37 eV with 0.2 eV FWHM and shoulders at 1.2 eV and 1.5 eV, respectively. The finding of activation energy in excess of O-O bond energy for the CC sites (in Table 3) is a result of the dynamic PD bleaching and creation process. This may also be observed through the negative probability frequency (thermally induced PD) peak at ≈1.1 eV for F1 and F3.

The F1 fiber shows peak activation energy at ≈1.6 eV by ≈0.1 eV FWHM which hold a similar trend relative to F2, F3 and the unspecified fiber in [13] of 1.5 eV in activation energy.

For F2 a peak at 1.36 eV and ≈0.2 eV FWHM is found which is to be compared to 1.3 eV and 0.5 eV FWHM in [12] where reaction rates for the various ramp anneals is applied to extract activation energy in relative relations among the various rates.

From Fig. 11(a) and Fig. 11(b) it appears that for Yb/Al material (F1, F3) the amount of thermally induced centers is larger than for Yb/Al/P material (F2). This is in the present implementation a result of different initial distributions on state II↑ and II↓, iii↑ or iii↓ for tetrahedral and octahedral CCs and that the P co-doped material not is expected to hold tetrahedral sites. The apparent increase in absorption for wavelengths in excess of 600 nm for Yb/Al/P in Fig. 8 is therefore mainly due to shift of the CC absorption center peaks with temperature as given by $R_*(\kappa,T)$ in Eq. (7).

The difference in pre-darkened distribution of states among the different fibers may be met by the model if it is assumed that there are internal temperature differences between tetrahedral and octahedral sites. Here a higher temperature is to be assumed for octahedral sites for a model with initially 50% population in state iii↓ and iii↑, respectively, such that after an isothermal anneal at temperatures from ≈350 K to ≈400 K the applied distributions may be found.

6. Conclusion

In this paper annealing of photo darkened rare earth co-doped silica material is described by means of a kinetic state model. It is proposed that the PD color centers are due to a σ-bond ("1") in parallel to a three electron bond (TEB) to Yb as "1+TEB" formed on = $Si<O_2$:·Yb. The bleaching of pre-darkened material goes reversibly through a "½" bond in parallel to a TEB to Yb and irreversible to TEB to Yb terminal states. The dissociation energies for resonant TEBs shared between = $Si<O_2$ and Yb^{3+} (or Al^{3+}) are determined by applying an analogy to ionic character bonds of molecular oxygen and superoxide.

The bleaching of "1+TEB" bonds formed on = $Si<O_2$ is modeled by a "fixated" phonon gas (SiO_4 ring structure) with characteristic frequency given by ring size and relative number of CC sites for Bose-Einstein phonon statistics. This results for fixed number of sites to a single element second order chemical reaction for phonon activation. Based on the kinetic state model cycles, ramps and isothermal anneal data are analyzed and it is shown that a common set of ionic character bond energies for "1+TEB" and "½+TEB" bonds formed on = $Si<O_2$ match the experimental data.

#187713 - $15.00 USD Received 25 Mar 2013; revised 7 May 2013; accepted 10 May 2013; published 17 May 2013